Full-dimensional accurate potential energy surface and dynamics for the unimolecular isomerization reaction $CH_3NC \rightleftharpoons CH_3CN$

Junlong Li,[1] Junhong Li,[1] and Jun Li[1*]

[1] School of Chemistry and Chemical Engineering & Chongqing Key Laboratory of Chemical Theory and Mechanism, Chongqing University, Chongqing 401331, China

*To whom correspondence should be addressed: jli15@cqu.edu.cn (JL).

Abstract

The reaction $CH_3NC \rightleftharpoons CH_3CN$, a model reaction for the study of unimolecular isomerization, is important in astronomy and atmospheric chemistry, and has long been studied by numerous experiments and theories. In this work, we report the first full-dimensional accurate potential energy surface (PES) of this reaction by the permutation invariant polynomial-neural network (PIP-NN) method based on 30,974 points whose energies are calculated at the CCSD(T)-F12a/AVTZ level. Then Ring Polymer Molecular Dynamics (RPMD) is used to derive the free energy barrier of the reaction at the experimental temperature range, 472.55 ~ 532.92 K. Reaction kinetics are studied in the high-pressure limit and in the fall-off region by standard transition state theory and master equation, respectively. The calculated temperature- and pressure-dependent rate coefficients are in good agreement with previous experimental and theoretical results. Further, Quasi-Classical Trajectory (QCT) simulations are performed on this PES to study the intramolecular energy transfer dynamics at initial vibrational energies of 4.336, 5.204 and 6.505 eV.

I. Introduction

Both methyl isocyanide (CH_3NC) and acetonitrile (CH_3CN) are detected in the interstellar space, and characterized by their rotational spectral lines due to their relatively small molecular size. These molecules thus usually served as valuable interstellar probes, and provide extensive insights into the physical and chemical conditions of the interstellar medium and contribute to our understanding of star formation processes within these cosmic regions.[1-4] Additionally, they are also detected in Earth's atmosphere.[5, 6] Relevant investigation is important for enhancing our comprehension of their atmospheric behavior, and lays a scientific foundation for air pollution control and risk assessment. Besides, the isomerization reaction between the two molecules, i.e., $CH_3NC \rightleftharpoons CH_3CN$, is an important prototype in the development of the unimolecular reaction theory.[7]

This isomerization reaction is favored in experiments due to its capacity to reduce the influence of side reactions and to be operated effectively at relatively low temperatures.[8-10] Schneider and Rabinovitch measured its thermal rate coefficient under high-pressure conditions, and the Arrhenius factor and the activation energy were determined to be $A = 10^{13.6}$ s^{-1}, $E_a = 1.665$ eV respectively from the two fall-off curves at 472.55 K and 503.55 K.[11] These findings were substantiated by subsequent studies that extend the rate coefficient across a broad range of temperatures and pressures. Fletcher et al. were the first to expand the study.[12] Then follow-up studies broadened the temperature from 393.15 to 593.15 K and the pressure from 2 to 100 Torr, which led to the refinement of the Arrhenius parameters.[13-15] Under such conditions, E_a was derived to be 1.656 ± 0.009 eV, while $\log_{10}A$ became 13.35 ± 0.11. Wang et al. investigated this reaction using advanced HeI photoelectron spectroscopy, and determined $E_a = 1.668 \pm 0.016$ eV. Besides, Reddy and Berry used a novel intracavity cw dye laser excitation technique to photoactivate CH_3NC with high state selectivity, measured the state-selected isomerization rate coefficient (at $E_a \approx 1.704$ eV).[16]

Since the 1970s, this isomerization reaction has been carried out by various computational methods, such as non-empirical self-consistent field SCF/DZ+P,[17, 18] many-body perturbation method SDQ-MBPT(4)/DZ+P,[19] a variety of density functional theory methods in junction with several basis sets,[20, 21] and high-level coupled-cluster calculations integrated with the Two Dimensional Master Equation (TDME).[22] These studies precisely calculated the structure of reactant, product, and transition state, as well as the minimum energy path (MEP), activation energy, reaction enthalpy and rate coefficient, which provide valuable insights into the title reaction.

The unimolecular reaction theory was founded and developed by Lindemann,[23] Hinshelwood,[24,

[25] Rice, Ramsperger, Kassel,[26-28] Marcus.[29, 30] Within the most sophisticated and preeminent Rice-Ramsperger-Kassel-Marcus (RRKM) theory, the vibrational degrees of freedom of reactants and transition states are typically treated quantum mechanically, while rotational and translational degrees of freedom are generally treated classically. Besides, it assumes that internal vibrational redistribution (IVR) is relatively fast and complete on the time scale of the unimolecular reaction. If IVR is slow, the initial rate coefficient will be microcanonical, while at later times this value will differ.[31, 32] The previous experimental results were aligned well with the RRKM predictions, indicating that CH_3NC is a textbook RRKM molecule.

However, the Hase group suggested a different perspective[33]: the CH_3NC may not be a standard RRKM molecule. They used direct dynamic simulations at the B3LYP/6-311++G(2d, 2p) level to study the unimolecular and intramolecular dynamics of the vibrationally excited CH_3NC. This process was found to deviate from the RRKM prediction, exhibiting nonexponential decay, which was intrinsic non-RRKM. Further, the dynamics at 4.336 eV excitation energy suggested that the Hinshelwood-Lindemann rate coefficient, $k_{uni}(\omega,E)$, aligned with the RRKM theory predictions under both high and low pressure limits, but deviated at intermediate pressures, where such deviation could be reconciled by introducing the scaling factor β_c.[33, 34]

Dynamic studies require a precise PES, which, to our knowledge, has not been developed for this system. This full-dimensional PES is capable of performing fast electronic structure calculations with a significant saving in cost compared to high-level electronic structure methods. It is also possible to carry out various dynamical calculations, exhibiting a great advantage over conventional direct dynamics method, which often struggles to achieve such high computational efficiency and accuracy at the same time. First, an extensive dataset of 30,974 data points is sampled and computed at the CCSD(T)-F12a/AVTZ level. The PIP-NN method[35-37] is then used for fitting, resulting in a total Root Mean Square Error (RMSE) of only 2.54 meV. Then the kinetics and dynamics calculations are performed using this PES. The rest of this work is organized as follows: Section II outlines the computational details of *ab initio* calculations, the PIP-NN fitting, kinetics and dynamics methods. Section III presents results and discussion, and Section IV concludes.

II. Method

1. Electronic Structure Calculation

For constructing a full dimensional accurate PES, the energies of all sampled points should be of high quality. To achieve this, it is essential to identify an electronic structure method that offers a

balance between accuracy and efficiency for all dynamically relevant regions. We finally choose the explicitly correlated coupled cluster single, double, and perturbative triple excitations with the augmented F12 explicit corrections,[38, 39] using the aug-cc-pVTZ basis set of Dunning,[40] CCSD(T)-F12a/AVTZ for short, as the theoretical method for all electronic structure calculations. CCSD(T)-F12a/AVTZ has the ability to efficiently obtain results as accurate as those obtained at the CCSD(T)/AV5Z level,[41] which has been widely used to develop PES for various systems, reactive or non-reactive.[42, 43] The T1 diagnostic values for most of the sampled points are consistently below 0.03, thus, a single-reference-based methodology seems to be appropriate for this reaction. All *ab initio* points are performed using the MOLPRO 2020 software package.[44-46]

2. PES

2.1 Sampling

To ensure full coverage of the dynamically significant configuration space, it is important to perform sampling as comprehensively as possible. In this work, we focus solely on one isomerization channel. To initiate the sampling, we propose to use the Ab Initio Molecular Dynamics (AIMD) simulation near the MEP to ensure that the main feature of the PES is captured.[47, 48] Also, selecting the right method for AIMD is crucial, just as choosing the method for electronic structure calculations is. However, the CCSD(T)-F12a/AVTZ method for AIMD simulations is impractical due to its expensive cost. In this work, we carried out a comparative analysis of various relatively low-level methods using the ORCA software package,[49] and the results are summarized in **Table 2**. The r2SCAN-3c method[50] yields comparable outcomes with the CCSD(T)-f12a/AVTZ method while taking less time. Hence, we select the r2SCAN-3c method to run AIMD simulations for the initial sampling.

It is worth noting that imbalanced dataset may deteriorate the performance and generalizability of machine learning model. Thus, to improve the quality of the dataset, the **isostat** program[51] is used to eliminate redundant points that show excessive similarity in both energy and geometry. This program uses a dual-threshold approach to screen for redundant configurations, considering both structure and energy: the configuration is retained only if it exceeds both predefined thresholds. To further improve the sampling efficiency, the generalized Euclidean distance metric is used to select points that are not too close to the existing dataset,[37]

$$\chi(r_i, r_i') = \sqrt{\sum_{i}^{15}(r_i - r_i')^2} < 0.4 - 0.7 \text{ Å}. \quad (1)$$

This distance metric is established based on the internuclear distances between a new point $\{r_i\}$ and a data point $\{r_i'\}$ in the existing data set. After completing this, it becomes possible to fit a primitive PES. Obviously, this PES is still rough, and further dynamical calculations are required to determine which region needs additional sampling. The procedure is done by several iterations to achieve convergence. Besides, its static characteristics are assessed by analyzing the results obtained from the PES and comparing with those from *ab initio* calculations to inspect if these regions are sampled sufficient.

2.2 PES Fitting

All of the *ab initio* points were fitted to a PIP-NN form with two hidden layers,[35-37]

$$V = b_1^{(3)} + \sum_{k=1}^{K}\left(\omega_{1,k}^{(3)} \cdot f_2\left(b_k^{(2)} + \sum_{j=1}^{J}\left(\omega_{k,j}^{(2)} \cdot f_1\left(b_j^{(1)} + \sum_{i=1}^{I}\omega_{j,i}^{(1)} \cdot G_i\right)\right)\right)\right), \quad (2)$$

where I denotes the number of the PIPs in the input layer; the hyperbolic tangent function are used for the activation function in the two hidden layers, denoted as $f_i (i = 1, 2)$; $\omega_{j,i}^{(l)}$ represents the weights connecting the ith neuron in the (l-1)th layer to the jth neuron in the lth layer; $b_j^{(l)}$ corresponds to the biases of the jth neuron in the lth layer. The optimal parameters ω and b are derived through an iterative process by nonlinear least-squares fitting of the Neural Network (NN) with the RMSE as a judgement criterion,

$$\text{RMSE} = \sqrt{\frac{\sum_{i=1}^{N_{\text{data}}}(E_{\text{fit}}^i - E_{\text{target}}^i)^2}{N_{\text{data}}}}. \quad (3)$$

The PIPs, denoted as $G = \hat{S}\prod_{i<j}^{6} p_{ij}^{l_{ij}}$, $p_{ij} = \exp(\frac{-r_{ij}}{\alpha})$ are the Morse-like variables, where α is an adjustable constant (in this study, α = 1.0 Å), and r_{ij} are the 15 internuclear distances. $\hat{S}$ includes all the possible permutation operations among the three hydrogen atoms and two carbon atoms in the C_2H_3N system. The PIPs of the system reach a maximum order of 5, $M = \sum_{i<j}^{6} l_{ij} \leq 5$, resulting in 1826 terms (I = 1826), are used as the input of the NN to ensure the adequate permutation symmetry of the system.

The entire data set was randomly divided into three distinct subsets: training (90%), validation (5%), and test (5%). The training set is used only for fitting purposes, while the validation set plays a crucial role in monitoring the training process. Additionally, the test set is used as an independent assessment of the fitting quality. To prevent overfitting in the NN training, the "early stopping" approach[52] is used by halting the training process when the performance on the validation set starts to degrade.

2.3 QCT calculation

The VENUS program[53] was used to perform QCT calculations on the PIP-NN PES to simulate the unimolecular isomerization dynamics. In these simulations, CH_3NC was excited with classical microcanonical sampling with specific total vibrational energies of 4.336, 5.204 and 6.505 eV, denoted as E_{vib}, while rotational energies were excluded. Such high vibrational energies are needed for the observation of sufficient amounts of isomerization within the time scale. The QCT simulations are time propagated without constraints, and terminate once $CH_3NC \rightarrow CH_3CN$ isomerization occurs, which is identified by inspecting the change of the CNC angle, as used in ref. [33]. At a CNC angle of 90°, the molecule is considered to reach the transition state and would not revert, which means recrossing of the trajectories back to the reactant is not considered in this work.[54] For each E_{vib}, 100,000 simulations are conducted, and plots of ln[N(t)/N(0)] vs. time are given for discussion, where N(t)/N(0) in this work represents the relative number of CH_3NC remaining vs. time.

2.4 Ring-polymer molecular dynamics (RPMD) calculation

To determine the free energy of the system along the reaction coordinate ξ and obtain reliable high-pressure limit rate coefficient, we used an advanced sampling technique known as umbrella sampling.[55] The methodology and theoretical framework are presented in detail in ref. [55], thus this work only provides a brief overview. This method is based on a stratification strategy that divides the range of the reaction coordinates into windows and applies a bias potential to confine the system to sample within each window. The bias potential typically has the form of a simple harmonic potential:

$$B_i(\xi) = \frac{1}{2}\mu_i(\xi - \xi_i)^2, \tag{4}$$

where μ_i is the elasticity coefficient of the ith window, and ξ_i is the value of the reaction coordinate at the center of that window. The bias potential modifies the probability distribution within each window and make it more uniform. Usually, the bias probability distribution $P_i(\xi)$ for each window can be obtained using conventional molecular dynamics or Monte Carlo methods. The weighted histogram analysis method[56] or integration method is then used to combine the probability

distributions from all windows. This integration results in the derivation of the global unbiased probability distribution $P(\xi)$ and the free energy distribution $A(\xi)$. Using the free energy obtained from the simulation, it is feasible to calculate the rate coefficient at the high-pressure limit:[54, 57, 58]

$$k(T) = \kappa \cdot \frac{k_B T}{h} \exp\left(-\frac{W(\xi_{TS}) - W(\xi_{min})}{k_B T}\right), \quad (5)$$

where T is the temperature, k_B is the Boltzmann constant, h is Planck's constant, $W(\xi_{TS})$ and $W(\xi_{min})$ are the free energies at the transition state and the reactant minimum, and κ is the time-dependent transmission coefficient. All the RPMD calculations were performed using the **Caracal program**.[59]

2.5 Master equation

Solving the kinetic master equation for the gas-phase system enables us to determine the temperature- and pressure-dependent reaction rate coefficients. The PES can quickly provide the geometries, frequencies and energies of the stationary points, which are required to obtain the microcanonical flux coefficients for the coefficient matrix in the master equation. The input data of master equation (including collisional parameters ε and σ) reported in refs[60, 61] are reused here and given in **Table 3**. The TUMME package[62, 63] was used to carry out all master equation calculations. The software begins by parsing a standard input file to retrieve global parameters, response data and species-specific attributes. Within this module, a symmetrized transition matrix is constructed and diagonalized. The process then ends with the output of rate coefficients and additional relevant information.

III. Results and discussion

3.1 Ab initio calculations

Figure 1 shows the reaction path diagram for this isomerization reaction, complemented by the optimized geometric parameters of the stationary points. Additionally, some prior theoretical results are included for comparison. As shown, the transition state involves the rotation of the methyl group, migrating from the nitrogen side of the cyano group to the carbon side (through a 1,2 methyl-shift), which results the breaking of the CN bond and the simultaneous formation of the CC bond. Namely, the structure transformation during the reaction is mainly featured through the angle θ_{CNC}. The molecule manifests as CH_3NC when θ_{CNC} reaches 180° and transitions to CH_3CN at 0°. CH_3NC and CH_3CN have nearly the same CH bond lengths for the methyl group, where these values are slightly lower than those obtained from the spectroscopic experiments,[64, 65] with a maximum deviation of

0.017 Å. And the three CH bond lengths in the methyl group do not remain the same in the transition state, but are slightly smaller than those in the reactant and product. The CN bond length of the cyano group increases by 0.023 Å from the reactant to the transition state and subsequently decreases by 0.037 Å from the transition state to the product, leading to an overall decrease of 0.014 Å. The CN and NC bond lengths are 1.424 Å, 1.172 Å for CH_3NC, while CH_3CN exhibits CC and NC bond lengths of 1.463 Å and 1.158 Å, respectively. These values are in good agreement with the experimental results,[66] 1.424 Å and 1.166 Å for CH_3NC, and 1.458 Å and 1.157 Å for CH_3CN.

For the energies of the stationary points, the HEAT-345Q results[22] are included in **Figure 1** for comparison. The PES is in good agreement with the CCSD(T)-F12a/AVTZ calculations, with a maximum deviation of only 0.003 eV at the transition state. All energies are relative to the CH_3NC if not specified hereafter and the PES energies do not include the zero-point energy. The barrier on the PES is 1.727 eV. With harmonic ZPE correction, the barrier becomes 1.651 eV, much close to the experimental result, 1.665 eV,[11, 13, 60] and the value calculated by HEAT-345Q with ZPE correction of 1.659 eV.[22]

The harmonic frequencies of the stationary points are listed in **Table 1** with results from available refs[18, 67, 68] for comparison. The PIP-NN PES accurately reproduces the *ab initio* calculation results with a largest deviation of only 18 cm^{-1} and in excellent agreement with the CCSD(T)/ANO2 results for the largest deviation of 19 cm^{-1}.[22] For the CH_3CN molecule, we compared the frequencies with the spectroscopic experimental data,[68] which includes anharmonic effect, and found that the two results are in reasonable agreement. In addition, anharmonic parameters were calculated by the vibrational perturbation theory[69] with the PIP-NN PES interfaced to the Gaussian program.[70-72] The results are shown in Supplementary Material in the low triangular form and compared with previous CCSD(T)/ANO1 results.[22] The RMSEs for the anharmonic rotational constants are 2.15 cm^{-1} for TS, 1.72 cm^{-1} for CH_3CN, and 3.65 cm^{-1} for CH_3NC, with corresponding mean absolute errors (MAEs) of 1.56 cm^{-1}, 1.57 cm^{-1}, 1.72 cm^{-1}, respectively, demonstrating its accuracy in studying the anharmonic effects by the PES but with greatly reduced calculation cost.

3.2 PES

According to our experience in the development of PES,[72-74] we firstly conducted an exhaustive examination of various NN parameters. With a comprehensive test, the NN's optimal architecture was identified. The architecture of the PIP-NN encompasses 1826 PIP terms as the input, with 10 neurons in each hidden layer, and a single potential energy output, resulting in 18,391 non-linear fitting

parameters. **Figure 2 (a)** depicts the sampled points as a function of θ_{CNC} and R_{CN}. One can see that the sampling covers sufficient range around the isomerization, where the R_{CN} extends from around 1.0 to 3.5 Å and θ_{CNC} varies from 0 to 180°. Besides, some scan points are added to the dataset to ensure adequate sampling in regions that are difficult to be sampled by AIMD. Clearly, the regions around the stationary points are sampled densely, and the MEP is also comprehensively covered. The contour of the PIP-NN PES is shown in **Figure 2 (b)**. The angle θ_{CNC} and the length R_{CN} are adjustable parameters while the other coordinates are fixed at the CH_3CN equilibrium. The PES not only provides an excellent description along the MEP, which is of primary interest, but also exhibits commendable performance in other high energy regions, demonstrating its reliability and accuracy.

The RMSEs for the total, training, validation, and test are 2.54, 1.91, 4.68 and 6.44 meV, respectively, with a maximum absolute error of 125.6 meV at 12.56 eV. The scattering plot of the fitting error as a function of the relative *ab initio* energy is represented in **Figure 3(a)**. One can see that the fitting errors for most data points are very small for an energy range up to 16 eV. Such high energy regions are necessary for the high energy simulations. **Figure 3(b)** presents the population of the absolute fitting errors: approximately 90% of the points exhibit absolute fitting errors within 0~1 meV, around 6% within 1~2 meV, and only 4% exceed 2 meV.

Figure 4 depicts the potential energy as a function of θ_{CCN}, which illustrates the process of 1,2-methyl shift with all other coordinates fixed at the CH_3NC equilibrium. Again, the potential on the PIP-NN PES is in excellent agreement with the *ab initio* results.

3.3 Kinetics calculations

The free energy and thermal rate coefficients of the title reaction were accurately determined with the PIP-NN PES interfaced to the **Caracal program**.[59] The reaction coordinate ξ corresponds to the reactant, transition state and product of the system at specific values of 0, 1, 2, respectively.[55] Thus, to ensure comprehensive sampling, a series of tests were conducted. Ultimately, the range of ξ from -0.05 to 1.95 was chosen. Note that the reaction coordinate at ξ = 1.875 corresponds to the product, rather than ξ = 2.0 as discussed in the method section. The umbrella sampling is performed in increments of $\Delta\xi$ = 0.01, resulting in 201 umbrella windows, and with the force constant of the bias potential of 0.05 (atomic units). The time step is selected to be 0.3 fs in all RPMD calculations. During the first step of generating initial structures, 5000 MD simulations are sampled for each window, where these trajectories are starting from the initial classical structure, and following 10000 MD steps

are calculated for equilibration with the specified RPMD beads. The Potential of Mean Force (PMF) is then computed across a range of partitions (bin = 5000) with the umbrella integration method. A set of tests were conducted to ensure that the results are converged with respect to the parameters, as presented in Supplementary Material. This analysis was carried out at three distinct temperatures (472.55 K, 503.55 K and 532.95 K), for which experimental data at the high-pressure limit are available.[11] To approximate the quantum mechanical results, convergence test with respect to the number of beads is carried out to determine the exact free energy.

Figure 5(a) provides a comparative analysis of the free energy using a set of beads: 1, 2, 4, 8, and 16 at 472.55 K. The calculated free energy barriers are summarized: 1.687 eV for 1 bead, and 1.672 eV for 2 beads. Subsequently we calculated with more beads to evaluate quantum effects. The free energy barriers are 1.655 eV for 4 beads, 1.655 eV for 8 beads, and 1.657 eV for 16 beads, respectively. One can see that the free energy barrier converged with 4 beads, beyond which the PMF results are nearly not changed. Hence, the free energy barrier is 1.655 ± 0.004 eV, which is slightly lower than the experimental value of 1.665 eV.[11, 13, 60] This difference can be neglected, as the experimental results are also of uncertainties. **Figure 5(b)** shows the time-dependent transmission coefficient κ at different beads, which is done to make sure that the rate coefficient is converged.

Next, the thermal rate coefficients k(T) at high-pressure limit were calculated at three temperatures (472.55 K, 503.55 K and 532.95 K). The results are shown in **Table 4**. At 472.55 K, 503.55 K and 532.95 K, k(T) is 6.13×10^{-5}, 7.16×10^{-4} and 7.52×10^{-3} s^{-1}, respectively. The SCTST/VPT2 results reported by Nguyen et al.[22] are included in **Table 4** for discussion. At 472.55 K, the RPMD result (6.13×10^{-5} s^{-1}) underestimates the experimental value (7.5×10^{-5} s^{-1}) with an error of 18.27%, while SCTST/VPT2 (8.9×10^{-5} s^{-1}) overestimates the experiment with an error of 18.67%. At 503.55 K, the RPMD result (7.16×10^{-4} s^{-1}) has an error of 22.6% compared to the experimental value (9.25×10^{-4}), with the SCTST/VPT2 outcome (1.1×10^{-03}) for the error of 18.9%. At 532.95 K, RPMD result (7.52×10^{-3} s^{-1}) nearly matches the experimental value (7.67×10^{-3} s^{-1}), with a minimal error of 1.96%, whereas SCTST/VPT2 calculation (9.7×10^{-3} s^{-1}) overestimates the experimental value by 20.9%. We also calculated the rate coefficients k(T, p) within the fall-off region and offered a direct comparison with Rabinovitch's experimental results[11] and TDME results by Nguyen et al.[22] As shown in **Figure 6**, all these results agree well over a wide range of temperatures and pressures, with temperatures ranging from 472.55 K to 532.95 K and pressures spanning from 10^{-2} Torr to approximately 10^{4} Torr. In the relatively low-pressure region (0.01~10 Torr), the rate coefficient k(T, p) increases sharply with

pressure. The ME and the experimental results are close to each other in this region, while 2DME slightly overestimate the experimental data. In the mid-pressure region (10~1000 Torr), the rate coefficients continue to rise but at a slower rate compared to the low-pressure region, and all theoretical and experimental results are in good agreement. At high-pressure region (above 1000 Torr), the rate coefficients reach a plateau, where further increasing in pressure has little effect on the reaction rate. Our ME calculation slightly overestimates the experimental and the 2DME results in this region. Overall, it confirms the accuracy of our theoretical model and its ability to predict kinetics behavior under wide temperature and pressure conditions.

3.4 Dynamics calculations

In this work, QCT simulations were carried out on the PIP-NN PES to simulate the dynamics of the unimolecular isomerization process. 100,000 trajectories were carried out with 4.336, 5.204 and 6.505 eV energy for initial E_{vib}, and 97.2%, 99.9% and 100% of the trajectories lead to isomerization. The RRKM theory[29] predicts that N(t)/N(0) follows an exponential decay: exp(-k(E)t), where k(E) represents the RRKM rate coefficient. According to the theory, if the reactants are randomly excited with E_{vib}, resulting in a microcanonical ensemble, then this ensemble will remain during the reaction and the reaction rate coefficient will be time independent. **Figure 7(a)** presents the natural logarithm of the relative number of CH_3NC molecules over time, ln[N(t)/N(0)]. The results by the direct dynamic simulations[33] are also included for comparison. The solid lines denote the prediction by the RRKM theory, with k(E) being 0.10, 0.32 and 0.92 ps^{-1} for E_{vib} at 4.336, 5.204 and 6.505 eV, respectively.[33] As depicted in the figure, the direct dynamic results, RRKM theory,[33] and QCT simulation are first close to each other. After a certain time, the direct dynamic results begin to deviate from the QCT simulations, which can be attributed to two key factors. First, the current PES is based on the high-precision CCSD(T)-F12a/AVTZ method, which is more accurate than the B3LYP/6-311++G(2d,2p) level employed in the direct dynamic simulations. Second, the direct dynamic simulations were limited to 150 trajectories for each E_{vib}, which are not sufficient and introduce large statistical errors.

In the case of a short period up to ~ 0.3 ps, the details of the QCT results are shown in **Figure 7(b)**. It can be seen that the QCT calculated lines can be apparently separated into two stages, as evidenced by the significant change of the slope. The corresponding rate coefficients for the first stage are 0.49, 1.10, and 2.76 ps^{-1}, respectively, which are lower than those observed in direct dynamic simulations, 3.1, 4.4, and 6.8 ps^{-1}.[33] Both direct dynamics and QCT simulations exhibit two distinct representations

for each E_{vib}. This unusual case complicates the classification of CH_3NC within the RRKM framework, suggesting that the molecule's dynamical behavior may not be fully captured by traditional RRKM theory. Theories, such as phase space theory,[75-79] may provide insights for it. Relevant investigations will be conducted in the near future.

IV. Conclusion

An accurate full-dimensional potential energy surface was developed for the isomerization of $CH_3NC \rightleftharpoons CH_3CN$. The configuration space relevant to this reaction was exhaustively sampled, accumulating a dataset of 30,974 points, each calculated by CCSD(T)-F12a/AVTZ. Subsequently, the PIP-NN approach was engaged to fit the PES, ensuring rigorous permutation symmetry. The final PES exhibits a total RMSE of 2.54 meV, demonstrating exceptional accuracy in reproducing the properties of the stationary points and the MEP. RPMD calculation was used to obtain precise free energy barrier for the reaction pathway, 1.655 ± 0.004 eV. Additionally, rate coefficients under the high-pressure limit were calculated and were in good agreement with the experimental values. The rate coefficients in the fall-off region were determined using master equation. Again, excellent agreement with experiment was achieved. All these findings suggested that the reaction was in excellent agreement with the predictions of the RRKM theory. QCT simulations were performed on the PIP-NN PES with initial E_{vib} of 4.336, 5.204 and 6.505 eV to study the dynamical behavior. Analysis of the relative amounts of reactants over time were conducted and compared with the predictions of RRKM theory and previous direct dynamic results. At each E_{vib}, two distinct decay patterns were observed, with reaction rates notably exceeding k(E) during the first initial short period. We speculate that this phenomenon may be related to the intramolecular mode coupling. High precision and reliable PES, that can accurately reproduce the experimental results of this thermal isomerization reaction and provide microscopic insights into the dynamics of non-RRKM, can be served as a reliable and efficient platform for further comprehensive dynamics.

Supplementary Material

Several tests about RPMD parameters: timestep, force constant, and child trajectories; anharmonic rotational constants for the stationary points.

ACKNOWLEDGEMETNS

We acknowledge the financial support from the National Natural Science Foundation of China

(Grants No. 21973009), Chongqing Talent Program (Grant No. cstc2021ycjh-bgzxm0070) and the Venture and Innovation Support Program for Chongqing Overseas Returnees (Grant No. cx2021071). Dr. Yang Liu is thanked for useful discussions.

AUTHOR DECLARATIONS

Conflict of Interest

The authors have no conflicts to disclose.

Author Contributions

Jun-Long Li: Conceptualization (equal); Data curation (lead); Formal analysis (lead); Investigation (equal); Writing – original draft (lead); Writing – review & editing (equal). **Jun-Hong Li:** Conceptualization (equal); Investigation (equal). **Jun-Li:** Conceptualization (equal); Supervision (lead); Writing – review & editing (equal).

DATA AVAILABILITY

The data that support the findings of this study are available from the corresponding author upon reasonable request.

Table 1. Comparison of the energies (in eV) and harmonic vibrational frequencies (in cm^{-1}) of the stationary points in the CH_3NC system.

Species	Methods	E	Frequencies											
			1	2	3	4	5	6	7	8	9	10	11	12
CH_3NC	PES [a]	0	262	262	955	1149	1149	1456	1503	1503	2197	3067	3154	3154
	Expt [b]	0	263	263	945	1129	1129	1429	1467	1467	2166	2966	3014	3014
	Ab initio [c]	0	262	262	956	1152	1152	1460	1504	1505	2200	3067	3155	3155
	Ab initio [d]	0	264	264	958	1153	1153	1460	1502	1502	2198	3068	3156	3156
CH_3CN	PES [a]	-1.047	363	363	924	1065	1065	1417	1489	1490	2303	3054	3148	3148
	Expt [e]	\	362	362	920	1041	1041	1385	1385	1448	2267	2954	3009	3009
	Ab initio [c]	-1.045	362	362	924	1063	1063	1416	1487	1487	2304	3066	3153	3153
	Ab initio [d]	-1.070	363	363	924	1062	1062	1415	1486	1486	2305	3067	3153	3153
TS	PES [a]	1.727	451i	178	641	988	1015	1320	1468	1474	1965	3088	3189	3241
	Ab initio [c]	1.730	451i	196	635	985	1000	1322	1475	1483	1971	3096	3198	3237
	Ab initio [d]	1.659	448i	195	637	989	996	1319	1473	1481	1966	3099	3203	3241
	Ab initio [f]	\	458i	255	677	1063	1083	1457	1590	1599	2189	3272	3388	3411

[a] This work, PIP-NN PES; [b] ref. [67]; [c] This work, CCSD(T)-F12a/AVTZ; [d] CCSD(T)-F12a/ANO2;[22] [e] Spectroscopy experiments;[68] [f] SCF/DZ+P.[18]

Table 2. Comparison of the bond lengths (in Å) of stationary points at different theoretical levels. Note the value of C-H is the average of the three CH bond lengths in the methyl group.

Notes	CH_3NC			CH_3CN			TS		
	C-H	C-N	C≡N	C-H	C-C	C≡N	C-H	C-C	C-N
CCSD(T)-F12a/AVTZ	1.087	1.424	1.172	1.088	1.462	1.158	1.082	1.782	1.839
B3LYP/def2-TZVP	1.089	1.418	1.164	1.090	1.454	1.149	1.082	1.801	1.845
PWPB95/def2-QZVPP	1.085	1.416	1.165	1.086	1.454	1.151	1.081	1.765	1.836
PWPB95/def2-TZVPP	1.086	1.416	1.166	1.086	1.454	1.152	1.081	1.768	1.832
r2scan-3c	1.094	1.418	1.170	1.075	1.539	1.147	1.086	1.801	1.819
revDSDPBEP86/ def2-QZVPP	1.082	1.422	1.155	1.082	1.463	1.140	1.076	1.761	1.895
ωB97X-2/def2-QZVPP	1.089	1.430	1.174	1.090	1.464	1.161	1.084	1.781	1.850

Table 3. Master equation parameters.

parameters	values
C_2H_6: bath gas[61]	mass = 30 g/mol, σ = 4.39 Å, ε/k_B = 234 K
CH_3NC/CH_3CN[60]	mass = 42 g/mol, σ = 4.47 Å, ε/k_B = 380 K

Table 4. Thermal rate coefficients (in s^{-1}) at the high-pressure limit for the isomerization of CH_3NC to CH_3CN.

Notes	T (K)		
	472.55	**503.55**	**532.95**
RPMD	6.13×10^{-05}	7.16×10^{-04}	7.52×10^{-03}
Experiment[11]	7.5×10^{-05}	9.25×10^{-04}	7.67×10^{-03}
SCTST/VPT2[22]	8.9×10^{-05}	1.1×10^{-03}	9.7×10^{-03}

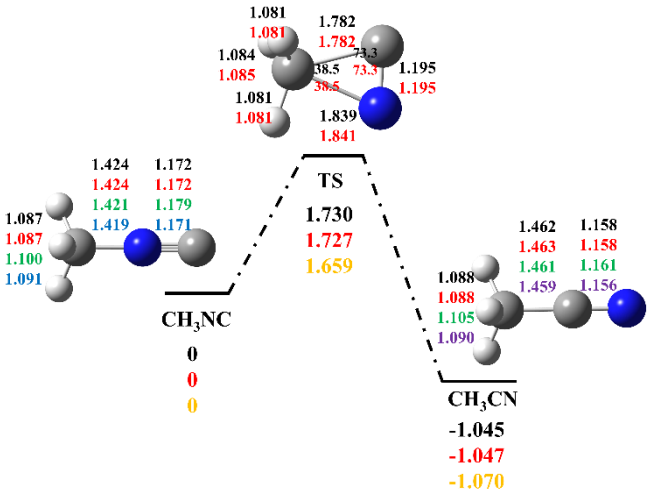

Figure 1. Schematic illustration of the reaction pathway, with energies (in eV), bond lengths (in Å) and angles (in °): black for CCSD(T)-F12a/AVTZ calculations, red for PIP-NN PES, green for B3LYP/cc-pVDZ,[21] blue and purple for microwave spectroscopy experiments,[64, 65] and yellow for HEAT-345Q protocol.[22]

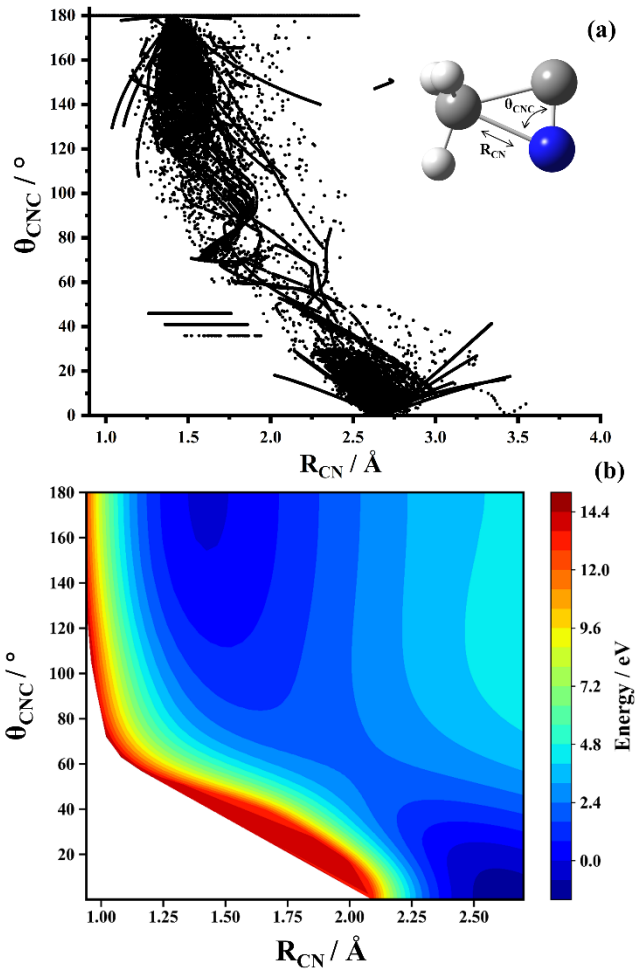

Figure 2. (**a**) Sampled points as a function of θ_{CNC} and R_{CN}. (**b**) Contour plot of the PES as a function of θ_{CNC} and R_{CN} with all other coordinates fixed at the CH_3CN equilibrium.

.

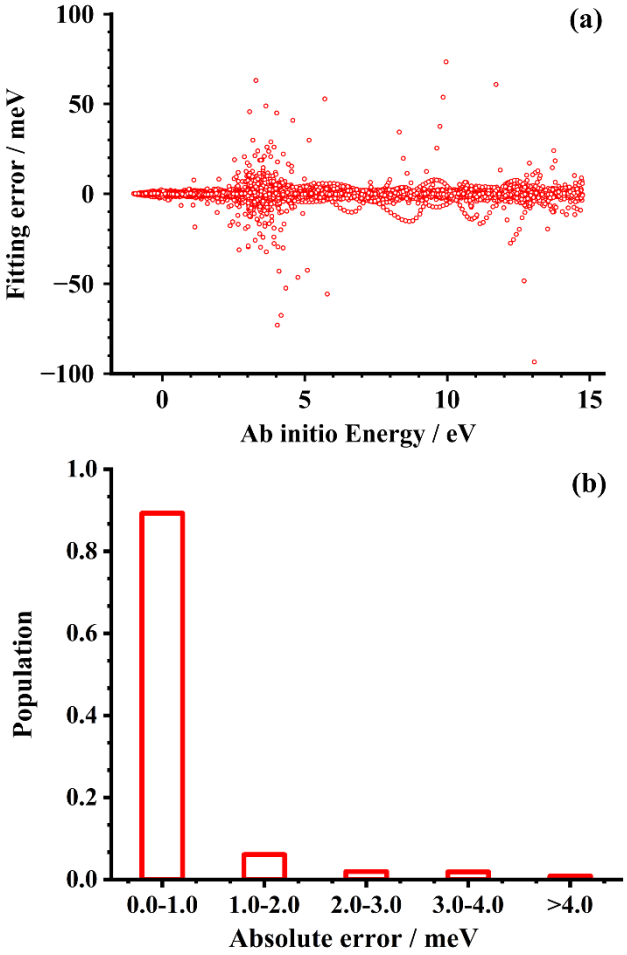

Figure 3. (**a**) Fitting errors (E_{fit}–E_{target}, in meV) of the PIP-NN PES as a function of the ab initio energy relative to the reactant CH_3NC. (**b**) Distributions of the absolute fitting errors.

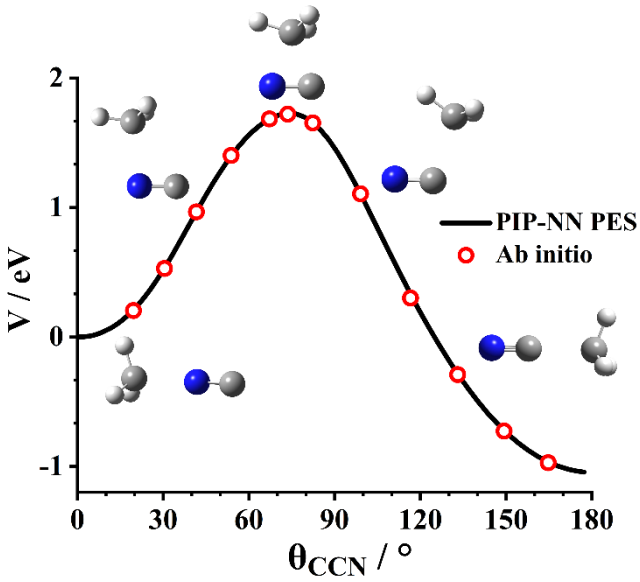

Figure 4. Comparison of potential energy between PIP-NN PES and ab initio results along the MEP.

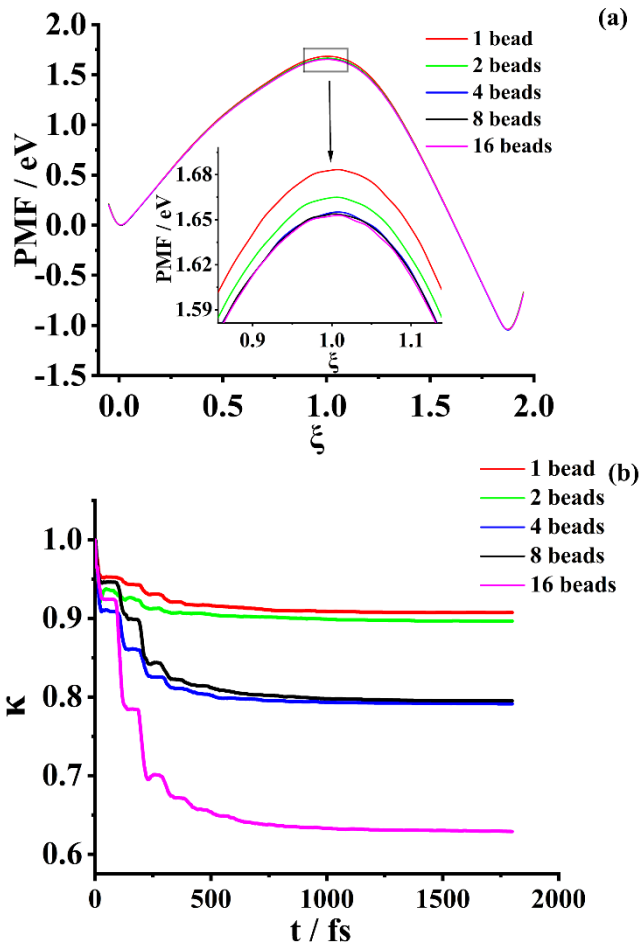

Figure 5. (**a**) Free energy changes along the reaction coordinate with different RPMD beads at 472.55 K. (**b**) Convergence of time-dependent transmission coefficient κ with different RPMD beads at 472.55 K.

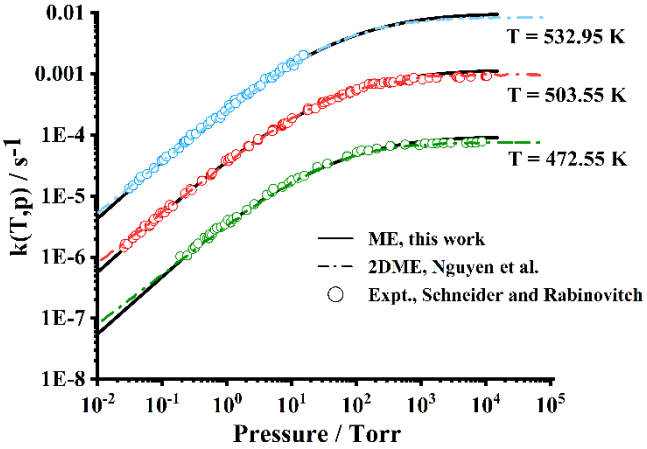

Figure 6. Temperature and pressure dependent rate coefficients calculated at three different temperatures (472.55, 503.55 and 532.95 K) in the fall-off region by the master equation based on the PIP-NN PES. Available experimental data[11] (circle symbols) and theoretical values[22] are included for comparison.

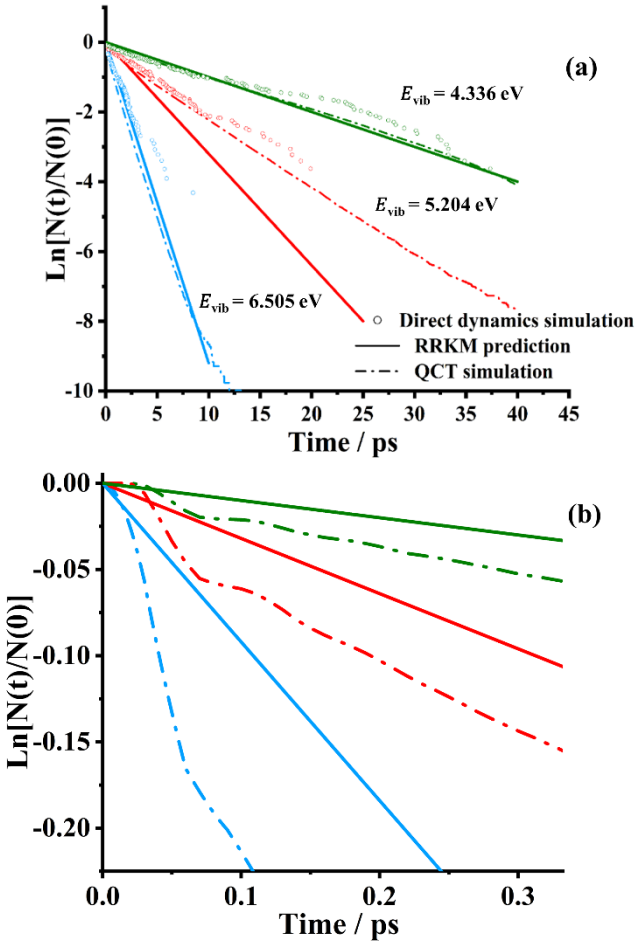

Figure 7. (**a**) Natural logarithm of the relative number of vibrationally excited CH_3NC molecules vs. time, i.e., N(t)/N(0). The blue, red, and green points are for initial microcanonical ensembles at 6.505, 5.204 and 4.336 eV, respectively.[33] The solid lines are the harmonic RRKM predictions.[33] (**b**) Natural logarithm of the relative number of vibrationally excited CH_3NC molecules vs. time, i.e., N(t)/N(0) for the initial short period.

References:

1. A. J. Remijan, J. M. Hollis, F. J. Lovas, D. F. Plusquellic and P. R. Jewell, Astrophys. J. **632** (1), 333-339 (2005).
2. A. M. Daly, C. Bermúdez, A. López, B. Tercero, J. C. Pearson, N. Marcelino, J. L. Alonso and J. Cernicharo, Astrophys. J. **768** (1) (2013).
3. P. Gratier, J. Pety, V. Guzmán, M. Gerin, J. R. Goicoechea, E. Roueff and A. Faure, Astron. Astrophys. **557** (2013).
4. I. Andron, P. Gratier, L. Majumdar, T. H. G. Vidal, A. Coutens, J. C. Loison and V. Wakelam, Mon. Not. R. Astron. Soc. **481** (4), 5651-5659 (2018).
5. H. P. Schuchmann and K. J. Laidler, J. Air Pollut. **22** (1), 52 (1972).
6. J. A. de Gouw, C. Warneke, D. D. Parrish, J. S. Holloway, M. Trainer and F. C. Fehsenfeld, J. GEOPHYS. RES-ATMOS. **108** (D11) (2003).
7. B. Peters, in *Reaction Rate Theory and Rare Events Simulations*, edited by B. Peters (Elsevier, Amsterdam, 2017), pp. 209-225.
8. R. G. Compton, C. H. Bamford and C. F. H. Tipper†, *Decomposition and Isomerization of Organic Compounds*. (Elsevier Science, 1971).
9. A. McAuley and W. E. Lindsell, in *Inorganic Reaction Mechanisms*, edited by A. McAuley (The Royal Society of Chemistry, 1979), Vol. 6, pp. 0.
10. M. L. v. Frenkel′, *Thermodynamic properties of isomerization reactions*. (CRC Press, 2020).
11. F. W. Schneider and B. S. Rabinovitch, J. Am. Chem. Soc. **84** (22), 4215-4230 (1962).
12. F. J. Fletcher, B. S. Rabinovitch, K. W. Watkins and D. J. Locker, J. Phys. Chem. **70** (9), 2823 (1966).
13. J. L. Collister and H. O. Pritchard, J. Phys. Chem. **54** (15), 2380-2384 (1976).
14. S. C. Chan, B. S. Rabinovitch, J. T. Bryant, L. D. Spicer, T. Fujimoto, Y. N. Lin and S. P. Pavlou, J. Phys. Chem. **74** (17), 3160-3176 (1970).
15. F. M. Wang and B. S. Rabinovitch, J. Phys. Chem. **78** (9), 863-867 (1974).
16. K. V. Reddy and M. J. Berry, Chem. Phys. Lett. **52** (1), 111-116 (1977).
17. D. H. Liskow, C. F. Bender and H. F. Schaefer III, J. Am. Chem. Soc. **94** (15), 5178-5182 (1972).
18. P. Saxe, Y. Yamaguchi, P. Pulay and H. F. Schaefer III, J. Am. Chem. Soc. **102** (11), 3718-3723 (1980).
19. L. T. Redmon, G. D. Purvis and R. J. Bartlett, J. Chem. Phys. **69** (12), 5386-5392 (1978).
20. B. S. Jursic, Chem. Phys. Lett. **256** (1-2), 213-219 (1996).
21. A. M. Halpern, J. Chem. Educ. **83** (1), 69 (2006).
22. T. L. Nguyen, J. H. Thorpe, D. H. Bross, B. Ruscic and J. F. Stanton, J. Phys. Chem. Lett. **9** (10), 2532-2538 (2018).
23. F. A. Lindemann, S. Arrhenius, I. Langmuir, N. R. Dhar, J. Perrin and W. C. McC. Lewis, Trans. Faraday. Soc. **17** (0), 598-606 (1922).
24. R. Marcelin, *Contribution a l'etude de la cinetique physico-chimique*. (Gauthier-Villars et cie., 1914).
25. W. H. Rodebush, J. Am. Chem. Soc. **45** (3), 606-614 (1923).
26. L. S. Kassel, J. Phys. Chem. **32** (7), 1065-1079 (1928).
27. L. S. Kassel, J. Phys. Chem. **32** (2), 225-242 (1928).
28. O. K. Rice and C. J. West, Annu. Surv. Am. Chem. **5**, 21-35 (1930).
29. R. A. Marcus, J. Chem. Phys. **20** (3), 359-364 (1952).
30. R. A. Marcus and O. K. Rice, J. Phys. Chem. **55**, 894-908 (1951).
31. D. L. Bunker, J. Chem. Phys. **37** (2), 393-403 (1962).
32. D. L. Bunker, J. Chem. Phys. **40** (7), 1946-1957 (1964).
33. B. Jayee, S. Malpathak, X. Ma and W. L. Hase, J. Chem. Phys. **151** (18) (2019).
34. P. W. Smith, B. Jayee and W. L. Hase, J. Phys. Chem. Lett. **11** (7), 2772-2774 (2020).
35. B. Jiang and H. Guo, J. Chem. Phys. **139** (5) (2013).
36. J. Li, B. Jiang and H. Guo, J. Chem. Phys. **139** (20) (2013).
37. B. Jiang, J. Li and H. Guo, Int. Rev. Phys. Chem. **35** (3), 479-506 (2016).

38. T. B. Adler, G. Knizia and H.-J. Werner, J. Chem. Phys. **127** (22) (2007).
39. G. Knizia, T. B. Adler and H.-J. Werner, J. Chem. Phys. **130** (5) (2009).
40. T. H. Dunning Jr, J. Chem. Phys. **90** (2), 1007-1023 (1989).
41. L. Kong, F. A. Bischoff and E. F. Valeev, Chem. Rev. **112** (1), 75-107 (2012).
42. M. Ben Khalifa, P. J. Dagdigian and J. Loreau, J. Phys. Chem. A. **126** (51), 9658-9666 (2022).
43. J. Li, Y. Liu, H. Guo and J. Li, Phys. Chem. Chem. Phys. **24** (44), 27548-27557 (2022).
44. H.-J. Werner, P. J. Knowles, G. Knizia, F. R. Manby, M. Schütz, P. Celani, W. Györffy, D. Kats, T. Korona and R. Lindh., Vol. 2023.
45. H.-J. Werner, P. J. Knowles, G. Knizia, F. R. Manby and M. Schütz, Wiley Interdiscip. Rev.: Comput. Mol. Sci. **2** (2), 242-253 (2012).
46. H. J. Werner, P. J. Knowles, F. R. Manby, J. A. Black, K. Doll, A. Hesselmann, D. Kats, A. Kohn, T. Korona, D. A. Kreplin, Q. L. Ma, T. F. Miller, A. Mitrushchenkov, K. A. Peterson, I. Polyak, G. Rauhut and M. Sibaev, J. Chem. Phys. **152** (14) (2020).
47. D. Marx and J. Hutter, *Ab initio molecular dynamics: basic theory and advanced methods*. (Cambridge University Press, 2009).
48. D. Marx, J. J. M. m. Hutter and a. o. q. chemistry, **1** (301-449), 141 (2000).
49. F. Neese, Wiley Interdiscip. Rev.: Comput. Mol. Sci. **2** (1), 73-78 (2012).
50. S. Grimme, A. Hansen, S. Ehlert and J.-M. Mewes, J. Chem. Phys. **154** (6) (2021).
51. T. Lu, (2023), Vol. 2023.
52. L. Raff, *Neural networks in chemical reaction dynamics*. (OUP USA, 2012).
53. W. L. Hase, R. J. Duchovic, X. Hu, A. Komornicki, K. Lim, D.-H. Lu, G. H. Peslherbe, K. N. Swamy, S. Vande Linde and A. Varandas, (1996).
54. D. G. Truhlar, B. C. Garrett and S. J. Klippenstein, J. Phys. Chem. **100** (31), 12771-12800 (1996).
55. J. Kästner, Wiley Interdiscip. Rev.: Comput. Mol. Sci. **1** (6), 932-942 (2011).
56. S. Kumar, J. M. Rosenberg, D. Bouzida, R. H. Swendsen and P. A. Kollman, J. Comput. Chem. **13** (8), 1011-1021 (1992).
57. P. Pechukas, Annu. Rev. Phys. Chem. **32** (1), 159-177 (1981).
58. K. J. Laidler and M. C. King, J. Phys. Chem. **87** (15), 2657-2664 (1983).
59. J. Steffen, J. Chem. Theory Comput. **19** (16), 5334-5355 (2023).
60. F. J. Fletcher, B. S. Rabinovitch, K. W. Watkins and D. J. Locker, J. Phys. Chem. **70** (9), 2823-2833 (1966).
61. H. Hippler, J. Troe and H. J. Wendelken, J. Chem. Phys. **78** (11), 6718-6724 (1983).
62. R. Zhang, X. Xu and D. G. Truhlar, Comput. Phys. Commun. **270**, 108140 (2022).
63. R. Zhang, X. Xu and D. G. Truhlar, Comput. Phys. Commun. **293**, 108894 (2023).
64. L. Halonen and I. M. Mills, J. Mol. Spectrosc. **73** (3), 494-502 (1978).
65. M. Le Guennec, G. Wlodarczak, J. Burie and J. Demaison, J. Mol. Spectrosc. **154** (2), 305-323 (1992).
66. C. C. Costain, J. Chem. Phys. **29** (4), 864-874 (1958).
67. S. Takehiko, (, National Institute of Standards and Technology, Gaithersburg, MD, 1972).
68. J. L. Duncan, D. C. McKean, F. Tullini, G. D. Nivellini and J. Perez Peña, J. Mol. Spectrosc. **69** (1), 123-140 (1978).
69. V. Barone, J. Chem. Phys. **122** (1), 14108-14108 (2005).
70. M. J. Frisch, G. W. Trucks, H. B. Schlegel, G. E. Scuseria, M. A. Robb, J. R. Cheeseman, G. Scalmani, V. Barone, G. A. Petersson, H. Nakatsuji, X. Li, M. Caricato, A. V. Marenich, J. Bloino, B. G. Janesko, R. Gomperts, B. Mennucci, H. P. Hratchian, J. V. Ortiz, A. F. Izmaylov, J. L. Sonnenberg, Williams, F. Ding, F. Lipparini, F. Egidi, J. Goings, B. Peng, A. Petrone, T. Henderson, D. Ranasinghe, V. G. Zakrzewski, J. Gao, N. Rega, G. Zheng, W. Liang, M. Hada, M. Ehara, K. Toyota, R. Fukuda, J. Hasegawa, M. Ishida, T. Nakajima, Y. Honda, O. Kitao, H. Nakai, T. Vreven, K. Throssell, J. A. Montgomery Jr., J. E. Peralta, F. Ogliaro, M. J. Bearpark, J. J. Heyd, E. N. Brothers, K. N. Kudin, V. N. Staroverov, T. A. Keith, R. Kobayashi, J. Normand, K. Raghavachari, A. P. Rendell, J. C. Burant, S. S. Iyengar, J. Tomasi,

M. Cossi, J. M. Millam, M. Klene, C. Adamo, R. Cammi, J. W. Ochterski, R. L. Martin, K. Morokuma, O. Farkas, J. B. Foresman and D. J. Fox, (Wallingford, CT, 2016).
71. X. Huang, J. Qin, J. Zhang and J. Li, Int. J. Chem. Kinet. **55** (8), 415-430 (2023).
72. X. Xu and J. Li, J. Phys. Chem. A. **126** (37), 6456-6466 (2022).
73. J. Jiang, J. Yang, Q. Hong, Q. Sun and J. Li, Chem. Phys. Chem. **25** (12), e202400078 (2024).
74. J. Li, Y. Liu, H. Guo and J. Li, Phys. Chem. Chem. Phys. **24** (2022).
75. D. L. Bunker and W. L. Hase, J. Chem. Phys. **59** (9), 4621-4632 (1973).
76. G. S. Ezra, H. Waalkens and S. Wiggins, J. Chem. Phys. **130** (16) (2009).
77. U. Lourderaj and W. L. Hase, J. Phys. Chem. A. **113** (11), 2236-2253 (2009).
78. M. Paranjothy, R. Sun, A. Kumar Paul and W. L. Hase, Z. Phys. Chem. **227** (11), 1361-1379 (2013).
79. B. Jayee and W. L. Hase, Annu. Rev. Phys. Chem. **71** (1), 289-313 (2020).